Earth Planet. Sci. Lett. 644 (2024) 118934

Contents lists available at ScienceDirect

Earth and Planetary Science Letters

journal homepage: www.elsevier.com/locate/epsl

The role of deformation on the early crystallization and rheology of basaltic liquids

Francesco Vetere [a,*], Sven Merseburger [b], Alessandro Pisello [c], Diego Perugini [c], Cecilia Viti [a], Maurizio Petrelli [c], Alessandro Musu [d], Renat Almeev [b], Luca Caricchi [d], Gianluca Iezzi [e], Michele Cassetta [f,g], Francois Holtz [b]

[a] Department of Physical Sciences, Earth and Environment, University of Siena, 53100, Italy
[b] Institute of Earth System Sciences (IESW), Leibniz Universität Hannover, Callinstrasse 3, 30167 Hannover, Germany
[c] Department of Physics and Geology, University of Perugia, Piazza Università 1, 06100 Perugia, Italy
[d] Department of Earth Sciences, University of Geneva, Rue des Maraîchers 13, CH-1205 Geneva, Switzerland
[e] Department of Engineering and Geology (InGeO), Università degli Studi "G. d'Annunzio", Chieti-Pescara, via dei Vestini 31, 66100 Chieti, Italy
[f] Department of Industrial Engineering, University of Trento, I-38122 Trento, Italy
[g] Department of Computer Sciences, University of Verona, I-37134 Verona, Italy

ARTICLE INFO

Editor: Dr C. M. Petrone

Keywords:
Etna
Basalt
Shear rate
Crystal growth rate
Viscosity

ABSTRACT

This study highlights the rheological variation of magmatic systems during the early crystallization stage, which undergoes very different shear stress. Etna basaltic glass, made from natural rock powder, was used as a starting material. Nine shear rate-controlled experiments were conducted at 1150 °C (below liquidus temperature and undercooling degree $\Delta T \sim 40$ °C) with shear rates ($\dot{\gamma}$) of 0.1, 1 and 10 s^{-1} using wide-gap concentric cylinder viscometry. Three additional experiments were conducted without spinning the melts (no shear, $\dot{\gamma} = 0\ s^{-1}$). Run-products were collected after 3, 6 and 9 h. The experiment with the highest shear rate ($\dot{\gamma}$=10s^{-1}) showed a brittle failure when viscosity reached the value of 2.90 log (Pa·s) and after ca. 1150s. The measured viscosity matches the shear stress at 7244 Pa, corresponding to the brittle failure in our partly crystallised system at these conditions. After 9 h, the response of the partly crystallised Etna basalt to different deformation rates results in decreasing viscosity from 4.89 to 3.83 and 2.90 (log Pa s) as the $\dot{\gamma}$ increases from 0.1 to 1 and 10 s^{-1}, respectively. The main outcome of this study relates to the nucleation and growth of minerals with shear deformation. The deformation-free ($\dot{\gamma} = 0\ s^{-1}$) runs show the presence of only two phases: glass and Fe-oxides (Fe-ox) with only a few vol% (1–3) of oxides crystals after 3, 6 and 9 h. The deformation-bearing ($\dot{\gamma} = 0.1$, 1 and 10 s^{-1}) runs show different scenarios: after 3 h, we observed only Fe-ox for a $\dot{\gamma}$ of 0.1 s^{-1} (similar to deformation-free ones). As the shear rate increases to 1 s^{-1} and 10 s^{-1}, solid phases after 3 h experiments are Fe-ox, plagioclase and clinopyroxene. Crystal growth rate depends on the applied shear rate: the highest rate is 1.1×10^{-6} cm/s and was measured for plagioclase after a 3 h experiment for $\dot{\gamma} = 10\ s^{-1}$. At $\dot{\gamma} = 0.1\ s^{-1}$, the plagioclase growth rate decreases to 2.70 and 1.35×10^{-6} cm/s as experimental time increases from 6 to 9 h, respectively. The vast range of shear stress and the systematic data obtained in this study are fundamental to deciphering crystallization dynamics suffered by magmas in volcanic reservoirs, dikes, conduits and lavas.

1. Introduction

How fast do melts react at subliquidus condition? How long do crystals nucleate and eventually grow in magmatic environments? How do crystals affect magma/lava rheology? Those questions are of fundamental importance to understand, model and foresee behaviours of magmas. In the last decades, scientists have spent much effort performing experiments and collecting data from field observations. Many experiments were conducted to track melt viscosity at isothermal conditions (Dingwell and Virgo, 1988; Dingwell, 1991; Richet et al., 1996; Whittington et al., 2000 and 2001). Fewer data are instead available for partially crystallized systems at isothermal conditions (Vetere et al., 2017, 2021, 2022; Kolzenburg et al., 2019; S. 2020; Vona et al., 2011, 2013; Di Fiore et al., 2023) and even less have been obtained by

* Corresponding author.
E-mail address: francesco.vetere@unisi.it (F. Vetere).

https://doi.org/10.1016/j.epsl.2024.118934
Received 15 April 2024; Received in revised form 18 July 2024; Accepted 6 August 2024

imposing representative cooling rate paths (F. Vetere et al., 2019 and F. 2020; Kolzenburg et al., 2018), which are relevant for dynamic systems. It is well established that at subliquidus conditions solid phases can develop with different sizes, shapes and volumes, and this can greatly affect the rheology of the system (Kerr and Lister, 1991; Mueller et al., 2010; Pistone et al., 2016; Arzilli et al., 2019; S. Kolzenburg et al., 2020 and reference therein). Moreover, for a crystalline content $\Phi < 60$ vol%, for dilute or semi-dilute regimes (where Φ varies between 0.05 and 0.25 and $\sim 0.25 < \Phi > \sim 0.6$ vol.%), mafic to intermediate systems are non-Newtonian possibly showing a shear thinning behaviour (Vetere et al., 2022 and reference therein). This characteristic can reduce the viscosity of magmatic systems and, therefore, influence the flow ability of rising magmas. Moving from the pioneering work of Kouchi (1986), another critical aspect concerns the absence or presence of deformation in a crystallising system; indeed, nucleation and crystal growth are progressively facilitated at high shear rates because it allows a continuous "*feed growth ingredients*" disposal (Vetere et al., 2021; Di Fiore et al., 2023). However, all these previous investigations were performed in a relatively narrow range of shear rates and terminated at a relatively high undercooling degree (ΔT) obscuring the early crystallization steps. The new results presented here from a series of concentric cylinder experiments clarify the role of shear rate (absence plus $\dot{\gamma}$ changing on three orders of magnitude from 0.1 to 10 $\dot{\gamma}s^{-1}$) on the crystallization of magmatic suspensions at relatively low subliquidus conditions, i.e. when nucleation begins. This new dataset is fundamental in modelling crystallization scenarios since the deformation of magmas can be highly variable.

2. Experimental and analytical methods

2.1. Starting material and glass preparation

The starting material selected for our experiments is a trachybasaltic scoria from the 2002–03 eruption collected from the scoria cones on the South flank of the South-East crater of Mt. Etna (Musu et al., 2023). Mt. Etna is one of the most active mafic volcanoes in the world (Branca et al., 2004; Cappello et al., 2013; Corsaro and Miraglia, 2022) and, along its history, has shown different eruptive styles, with increasing explosiveness during the last period (Behncke and Neri, 2003; Branca and Carlo, 2005; Cappello et al., 2013). The product chosen for this study is among the most primitive ever erupted in recent history (Andronico et al., 2005). Thus, crystallization experiments are run on the composition, possibly reflecting a primitive magma at Mt. Etna.

The calculated liquidus temperature for our starting composition is 1188 °C (PhasePlot version 2.0.1 from M. Ghiorso); accordingly, the starting glass was prepared by powdering and melting the basaltic scoria at a significantly higher temperature of 1400 °C for 4 h to remove any possible solid phase and bubble (Vetere et al., 2013). The crucible hosting the powdered rock/glass is made of Pt and melting was performed in a Nabertherm HT 04/17 MoSi2-heated box furnace (Nabertherm GmbH, Lilienthal, Germany). Then, the melt was rapidly quenched into glass by pouring it on a brass plate. The resulting glass was powdered, remelted and quenched again as described above. The adopted quenching procedure allows us to get a homogeneous glass, avoiding the occurrence of quenched crystals (Vetere et al., 2015, 2017; F. 2019). The obtained starting glass composition is reported in Table 1).

The starting glass chemical analyses were acquired using a JEOL 8200 Superprobe at the University of Geneva conducted using a defocused beam set to 10 μm, with 15 KeV acceleration voltage and a beam current of 6 nA. Residual glasses and solid phase compositions were acquired at Hannover using a JEOL JXA-iHP200F Hyper Probe equipped with a field emission gun. For glass analysis, a defocused beam was set to 12 μm with an acceleration voltage of 15 kV and 10 nA. A focused beam of a few units of μm was set for all mineral phase analyses with 15 kV and 15 nA. Standardization was done at the beginning of each measuring day on well-known minerals and certified standards, with an acceptable deviation of <1 %.

2.1.1. Viscosimeter measurements protocol

Viscosity measurements have been performed in a Gero HTRV 70–250/18 high-temperature tube furnace with $MoSi_2$ heating elements (Gero GmbH, Neuhausen, Germany) operating up to 1800 °C at atmospheric pressure. Temperature can be precisely controlled via computer using the Eurotherm iTools v. 9.57.11 software (Eurotherm, Worthing, West Sussex, UK). This furnace can move vertically using two pneumatic cylinders allowing: (1) a precise positioning of outer and inner cylinders outside the furnace; (2) very fast heating of the sample by moving up the pre-heated furnace around the crucible previously positioned. In particular, the cylindric crucible is made of Pt_{80}-Rh_{20} with an inner diameter of 37 mm (outer diameter of 40 mm) and height of 70 mm. This setup allows us to work and experimentally investigate ~50 cm^3 of melts + crystals. The viscometer utilized is a rotational Anton Paar RheolabQC viscometer head installed at the Petro-Volcanology Research Group laboratories of the University of Perugia (hereafter PVRG lab) that allows recording viscosity in the range from 0.1 to 10^6 Pas with an accuracy of ± logη=0.03 Pas (Morgavi et al., 2015; F. Vetere and Holtz, 2020; Vetere et al., 2021). A calibration measuring the NIST 717 standard glass and Wacker silicone having a viscosity of 10 and 1000 Pa s (Spina et al., 2016a, 2016b; Vetere et al., 2017) was performed before the experimental runs. The procedure for viscosity measurements is

Table 1
Microprobe analyses of starting and residual glasses.

	SiO_2	TiO_2	Al_2O_3	FeO	MnO	MgO	CaO	Na_2O	K_2O	ρ (kg/m^3)
Starting glass	48.71	1.77	16.55	10.32	0.18	6.17	10.89	3.45	1.96	2.725
SR0.0–3h	50.61	1.83	17.32	7.71	0.17	5.86	11.11	3.16	2.21	2.664
SR0.0–6h	49.58	1.68	17.25	9.56	0.17	5.98	10.32	3.16	2.29	2.682
SR0.0–9h	49.88	1.79	17.36	8.56	0.18	5.95	10.80	3.11	2.16	2.676
SR 0.1–3h	50.50	1.72	17.67	7.23	0.22	6.02	10.90	3.51	2.07	2.679
SR 0.1–6h	51.08	1.93	16.24	7.41	0.20	6.64	10.44	3.54	2.39	2.682
SR 0.1–9h	50.81	1.86	16.24	7.71	0.27	6.75	10.16	3.61	2.44	2.685
SR 1–3h	52.28	2.01	16.68	6.86	0.24	5.92	8.87	4.09	2.86	2.654
*SR 1–6h**	*52.63*	*2.08*	*16.67*	*6.68*	*0.25*	*5.96*	*8.41*	*4.21*	*2.99*	2.647
SR 1–6h	52.10	2.09	16.24	7.35	0.20	6.00	9.67	3.50	2.82	2.667
SR 1–9h	52.17	2.05	16.60	6.93	0.22	5.96	9.01	4.06	2.82	2.657
SR 10–3h	51.58	2.01	16.60	7.27	0.23	6.24	9.30	3.95	2.69	2.667
SR 10–6h	52.57	2.10	16.63	6.72	0.23	5.79	8.68	4.11	2.97	2.649
SR 10–9h	52.89	2.16	16.71	6.49	0.22	5.70	8.42	4.24	3.02	2.643

EPMA analyses on the starting composition were performed at the Dept. Earth Sciences, University of Geneve (CH), while analyses on experimental products were performed at the Dept. Mineralogy, University of Hannover (DE). Standard deviations (1σ) are within 0.4 for SiO_2, Al_2O_3, FeO and CaO while within 0.1 for all the other presented oxide data. Measurements are an average of 20 single points. Glass density (starting material and residual glasses) was estimated using the model of Klöß (2000).

reported in supplementary material and Figure S1.

Finally, the rotational viscometer allows measurements under controlled $\dot{\gamma}$. This gives us the possibility to investigate the shear effects on viscosity of melts and partly crystallized systems.

At the end of each experiment, the crucible was quenched by moving it into the cooled head of the furnace. The quench rate was on the order of 100 °C/min. Sampling was performed by drilling out the closest portion (by using a diamond drilling bit) to the spindle to highlight the maximum possible effect of shear stress on crystal nucleation and growth processes. In fact, the imposed shear rate depends on the distance from the spindle with a maximum rate closest to the spindle and almost zero rate closest to the crucible wall (Mezner, 2014).

In magma chambers $\dot{\gamma}$ is estimated to be in the order of 10^{-9} s^{-1} (Nicolas and Ildefonse, 1996), while during transport in lava flows, dikes and conduits, the shear rate varies from ~70 s^{-1} (i.e. Plinian eruptions; Papale, 1999) down to 2.5–0.001 s^{-1} (i.e. in lava flows; Piombo and Dragoni, 2009; Cashman et al., 2013; Kolzenburg et al., 2018).). Accordingly, we selected shear rate values as much as possible as variables on the lab scale, i.e., 0.1, 1 and 10 s^{-1}. To complement them, the same three cooling experimental paths (heating up to 1400 °C, cooling to 1150 °C and then 3, 6 and 9 h at this temperature) were investigated without shear stress, i.e. $\dot{\gamma}$ equals to 0 s^{-1}.

2.2. Analytical protocol

All the quenched samples were prepared on thin sections for SEM and EPMA investigations. The BSEs were collected at the Institute of Mineralogy (University of Hannover) using a Jeol JSM-7610FPlus with 15 keV acceleration voltage and 10 nA beam current. The working distance was set to 15 mm for collecting large maps by stitching single BSE microphotographs at 250x to better reproduce the textures of run-products, i.e. large and tiny crystals (Fig. 1). Major-element contents of the experimental glasses and crystals were determined using a JEOL *JXA-iHP200F* field emission electron microprobe hosted at the Leibniz Universität Hannover. Glasses were measured with a defocused beam (15 kV; 10 nA; 12 μm size). Crystals were measured with 15 kV and 15 nA using a focused beam. Counting times were 10 s on peak and 5 s for the background for Na and K. For all other elements we applied 20 s on peak and 10 s for the background. Sodium and potassium were always measured first to mitigate alkali migration during analysis.

Thirteen thin sections were prepared: 1 for the starting glass, 3 for each investigated time- deformation-free run and 9 for each investigated time-shear rate run. Samples were named considering the shear rate applied and the dwell time of the experiment (e.g. SR 1–3 h means Shear Rate =1s^{-1} for 3 h; see Table 1). In particular, at 1150 °C we performed: a) 3 run-products solidified at 0, 0.1, 1 and 10 s^{-1} and for 3 h, b) 3 run-products solidified at 0, 0.1, 1 and 10 s^{-1} for 6 h and finally c) 3 run-products solidified at 0, 0.1, 1 and 10 s^{-1} for 9 h.

2.3. Image analyses

A total of 19,036 BSE images were collected to attain a clear and statistically relevant dataset for all the experimental runs. Image analyses were performed by using the Image ProPlus software to determine phase abundance and distribution in each run product; the applied analytical protocol of image analysis is the same as reported in Iezzi et al. (2008, 2011) and Vetere et al. (2013, 2015) where the identification of phases was determined by linking their grey-level ranges with the compositions.

3. Results

3.1. Qualitative textures

The crystalline phases observed in our experiments are Fe oxides (Ox), plagioclase (Plg), and clinopyroxene (Cpx) in various proportions, depending on the applied shear rate. Fig. 1 shows deformation-free and deformation-bearing run products and mineral phases. For deformation-free run, only glasses and Fe-ox were detected (sample named SR0-xh), whereas the 9 deformation-bearing run, and related solidified phases, are dependent on experimental duration (3, 6 and 9 h, respectively) and applied shear rate. The only evident contrasting experimental product was observed in the SR1–6h* run. In fact, as also visible in Fig. 1, it seems that this run shows higher crystallinity when compared with the SR1–9 h run at an identical shear rate. Both the experimental products obtained at a $\dot{\gamma}$ of 1s^{-1}. This difference is attributed to fluctuation in temperature (1144 ± 5 °C) that possibly favors the nucleation/growth rate (Vetere et al., 2013). Thus, we repeated this run (SR1–6 h), and the results are consistent with the experiments performed at lower and higher shear rates; consequently, as also shown in literature, thermal cycling affects the appearance and growth of solid phases in silicate melts (Erdmann and Koepke, 2016; Mills and Glazner, 2013).

3.2. Chemistry of phases

The compositions of the starting and residual glasses are reported in Table 1. In terms of SiO_2 content, it is evident that as $\dot{\gamma}$ increases from no shear to the highest shear rate (0–10 s^{-1}), the SiO_2 content increases from 48.7 (starting material) to 53.4 wt% (SR_10–9 h) while FeO, CaO, MgO decrease and Na_2O plus K_2O increases, due to solid phase crystallization.

Plagioclase does not appear at the deformation-free and lowest shear rate at 3 h; i.e. SR_0–3 h and SR_0.1–3 h runs, but it is present in all the deformation-bearing runs. **Table S1** and **Figure S2** show no clear chemical shift of Plg as time and shear stress vary since its compositions are invariably close to An_{68}, excepting a slight compositional change at 10 s^{-1}. Cpx compositions are shown in **Table S2** and **Figure S3**. Relative differences rely on run-product at 0.1 s^{-1} as time increases from 6 to 9 h. On average, the En content increases from ca. 36 to ca. 39 mol.% and Fs content decreases from 18 to 16 mol.%, whereas Wo content remains almost constant and close to ca. 46 mol.%.

As the shear rate increases to 1 s^{-1} and time proceeds from 3 to 9 h, compositions are more variable moving on average from $En_{36}Wo_{43}Fs_{21}$ to $En_{46}Wo_{42}Fs_{12}$. At 10 s^{-1}, composition variability is less pronounced (**Table S2–1 and Figure S3**).

However, all the samples show Cpx with variable BSE grey levels that indicate chemical zoning. To better characterize the Cpx chemical variation, we performed detailed EPMA analyses as presented in Table S2–2. These analyses evidence that Cpx showing chemical zoning (dark to bright grey levels) have clearly two compositional clusters: one is more En-rich and the other more Wo-rich (**Table S2–1 and Figure S3**).

Fe-oxide compositions are close to magnetite and even a slight shift toward hematite composition is evident for the highest applied shear rate. Interestingly, Fe-oxides crystallized in runs with $\dot{\gamma} = 0$ s^{-1} are identical in composition to the highest shear rate runs (**Table S3 and Figure S4**).

Concerning the residual glasses, we observe an increase in the SiO_2 content as the applied shear rate increases. For example, for the 9 h runs, Table 1 clearly shows that the SiO_2 content increases from 49.9 to 50.9 to 52.2 and 52.9 wt% as the shear rate increases from 0 to 0.1, 1 and 10 s^{-1}, respectively. Note that the starting material has a SiO_2 content of 48.7 wt% (Table 1).

Glass compositions are shown in Fig. 2 where SiO_2 is plotted vs CaO for the deformation-free runs and the three investigated shear rates at 9 h. The 9 h experiments show a decrease of the FeO content from 10.3 to 8.6, 7.7, 6.9 and finally 6.5 wt%, as the shear rate increases (Table 1). This behaviour is due to the crystallization of Fe oxide (Fig. 1). Na_2O and K_2O increase as the shear moves to high rates; at the highest shear rate, their sum is about ~ 1 wt% in the residual melt (compare starting material and SR 10–9 h in Table 1).

However, for a $\dot{\gamma}$ of 0.1s^{-1} we found only one small Plg crystal in all

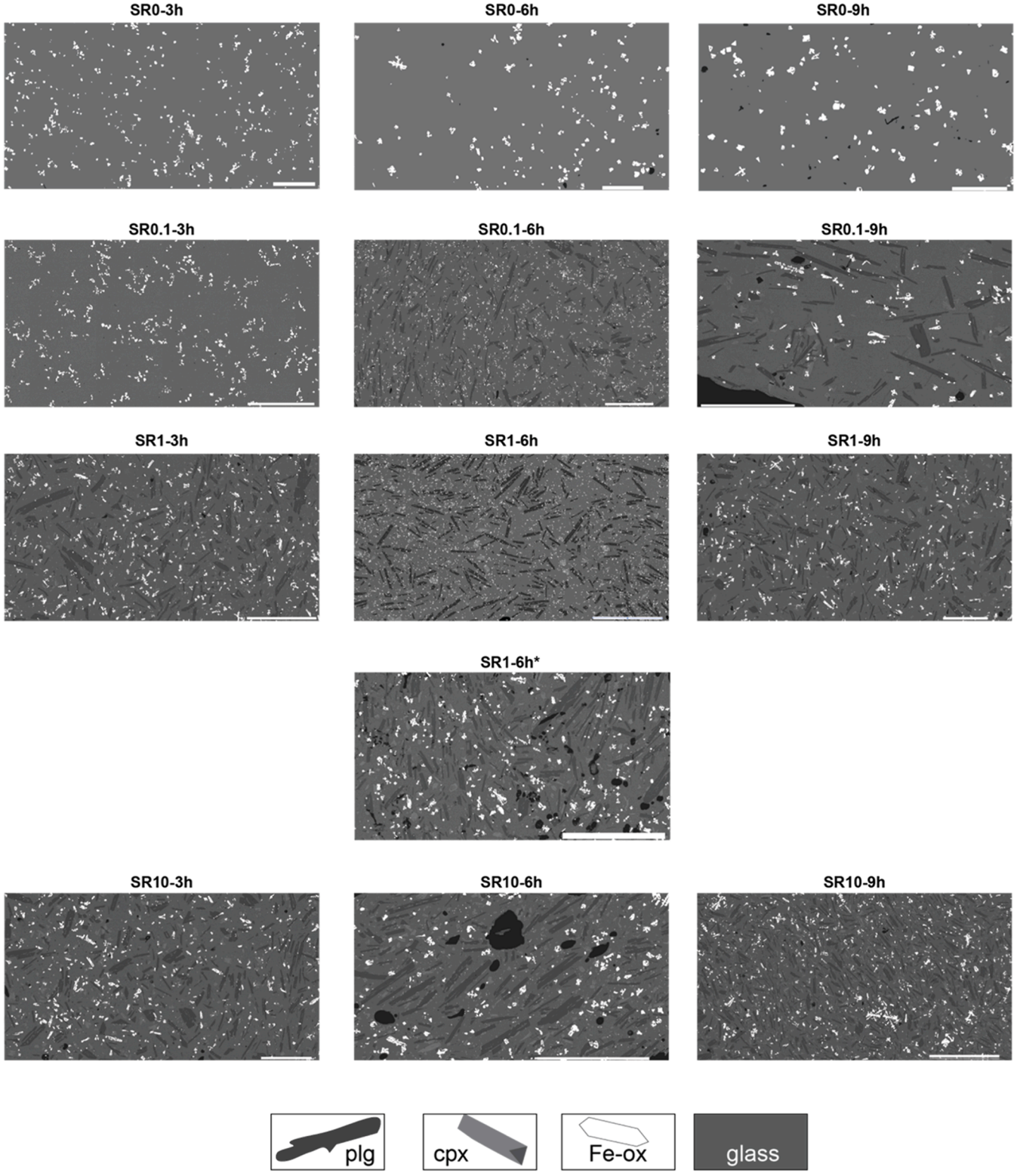

Fig. 1. Textural features of the 12 + 1 experimental runs solidified at variable shear rates and experimental duration. Magnification was chosen to obtain a representative and accurate view of textural attributes of the four detected phases: dark grey for Plg, middle grey for glasses, light grey for Cpx and white for Fe-oxides. SR0 images are the three deformation-free experiments after 3, 6 and 9 h run duration, respectively. The only detected phases are Fe-oxides, white color (2–4 vol%) and glasses in grey. Note the comparison between experimental products at $1s^{-1}$ for 6 h. Run suffering thermal cycling is named SR1–6h* (see text for details). White scale bars are 500 μm. The black domains are holes filled with glue during thin sections preparation. The collected BSE images are, in total, 19,5036 and only a representative part of each mosaic is shown here.

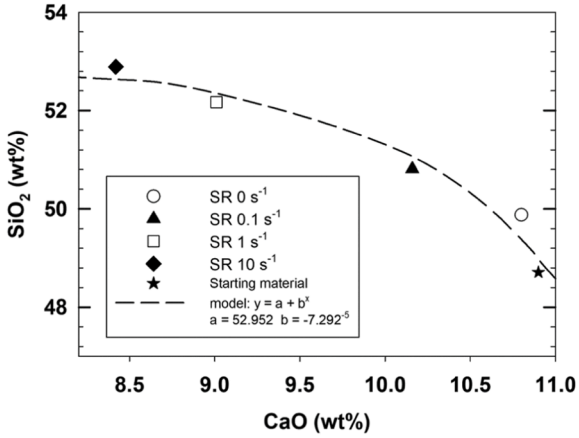

Fig. 2. Note: SiO_2 vs CaO in the glasses obtained after the 9 h runs at shear rates of 0, 0.1, 1 and 10 s^{-1}. Note that the SiO_2 content increases as the applied shear rate increases; a comparison with the starting material is also provided. Errors are smaller than symbols. R^2 is 0.96.

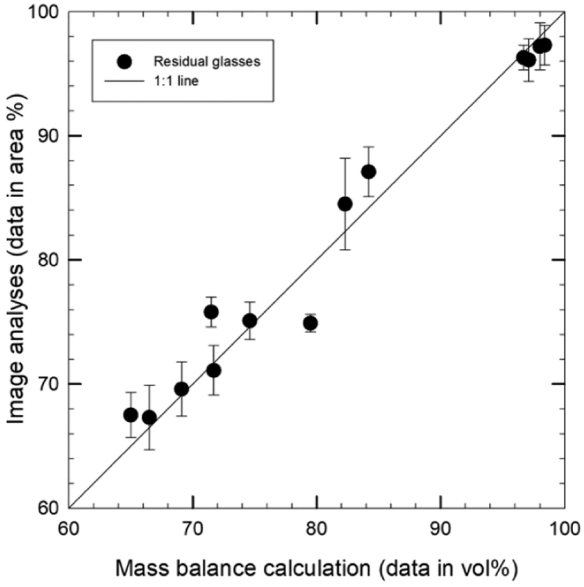

Fig. 3. Mass balance calculation vs image analysis approach is used to determine the proportion of residual glasses in all the experimental runs.

the 1914 BSE images, suggesting that three hours are necessary to begin the crystallization of Plg under these conditions. In agreement, at the same shear rate, Plg and Cpx are more numerous after 6 h.

As the shear rate increases to $1s^{-1}$, the solidification phases change. After 3 h, we have Fe-oxides plus Plg; further increases of the shear rate to 10 s^{-1} cause the appearance of all the 3 solid phases mentioned so far (Fe-oxides, Plg, and Cpx) plus the residual glass (Table 2 and Fig. 1).

3.3. Image analyses and mass balance

Fig. 1 shows selected BSE images and representative parts of each mosaic. Results based on measurements of thousands of crystals are reported in Table 2 as area%. Image analyses allow us to evaluate the aspect ratio of solid phases (*AS* = major axis/minor axis) as shear rate and time vary for all the experimental run. Plagioclase is elongated with AS > 4 on average for all the experimental runs. On average, AS for Cpx is < 3 and finally Fe-ox present the lower AS value always close to 2, independently on the applied shear rate (please refer to supplementary Figures S5.1 and S5.2).

Amount phases computed by mass balance using the GeoBalance program (Li et al., 2020) and image analysis are in good agreement as directly observable in Fig. 3. The proportions of residual glasses derived by the two methods are plotted in Fig. 3.

The residual melts in **SR 0.1–6 h** show the maximum difference between image analysis and mass balance of <5 %.

It is worth mentioning that the data derived by using the mass balance calculations are reported in vol% by converting the mass in volume by using the appropriate density for all the phases (Plg: 2.5 g/cm^3; Cpx: 2.9 g/cm^3; Fe-oxide: 3.9 g/cm^3; glasses: see Table 1). Major differences between solid phases calculated via mass balance and via image analysis reside on Cpx. Image analysis for some samples (SR1_3 h and SR10–9 h) underestimates the mass balance by <7 % (Table 2).The evolution of residual melts, Plg, Cpx and Ox at different shear rates is shown in Fig. 4 (data in Table 2), together with the sample that suffered thermal cycling (triangle in Fig. 4). The proportion of all solid phases increases with increasing shear rate and run duration.

Our experiments provide information on Fe-oxide, Plg and Cpx growth rates calculated by averaging the length of the long axis of the 10 largest crystals (L) and dividing by the experimental time ($G = L/t$; Hammer and Rutherford, 2002; Couch, 2003; Arzilli et al., 2016; Iezzi et al., 2011). In addition, following Vetere et al. (2021) and Chevrel et al. (2015) we have used the following expression to retrieve the maximum and the average growth rate: $G = 0.5\ x\ L/t$. Here we assume a constant G over time.

The length of all the crystals acquired via image analyses process was used to build up Table 3 and Fig. 5 reporting the growth rate and the appearance of all solid phases related to experimental run time for the 9

Table 2
Image analyses and mass balance results.

			Image analyses								mass balance			
BSEs #	$\dot{\gamma}$ s^{-1}	time h	glass area%	std	Plg	std	Cpx	std	FeTiox	std	glass vol%	Plg	Cpx	FeTiox
1223	0	3	96.1	1.7	0.0	0.0	0.0	0.0	3.9	0.6	97.1	0.0	0.0	2.9
1914	0.1	3	96.3	1.0	0.1	0.1	–	–	3.7	0.5	96.7	–	–	3.3
1188	1	3	75.8	1.2	13.8	0.2	6.1	0.1	4.3	0.5	71.5	12.1	12.9	3.5
1323	10	3	75.1	1.5	14.0	0.3	6.7	1.4	4.2	0.5	74.6	11.4	10.7	3.3
1756	0	6	97.3	1.6	0.0	0.0	0.0	0.0	1.1	0.5	98.4	0.0	0.0	1.6
2094	0.1	6	87.1	2.0	11.0	2.2	0.4	0.1	1.5	0.9	84.2	8.7	3.8	3.3
870	***1***	***6***	***67.5***	***1.8***	***19.4***	***1.8***	***8.0***	***1.3***	***5.2***	***1.3***	***65.0***	***17.2***	***13.5***	***4.2***
1517	1	6	74.9	0.7	15.0	0.8	5.6	0.8	4.0	0.5	79.5	13.3	7.11	0.1
1281	10	6	69.6	2.2	17.9	1.1	7.6	1.5	4.9	0.4	69.1	13.4	13.5	3.9
1172	0	9	97.2	1.9	0.0	0.0	0.0	0.0	2.8	0.4	98.0	0.0	0.0	2.0
1926	0.1	9	84.5	3.7	10.7	2.2	1.8	1.5	3.2	0.5	82.3	10.2	4.4	3.1
1428	1	9	71.1	2.0	16.5	1.9	8.0	1.4	4.4	0.5	71.7	12.6	12.0	3.8
1344	10	9	67.3	2.6	18.7	2.2	8.2	1.9	5.9	0.32	66.5	14.7	14.8	4.0

Image analyses results and comparison with mass balance calculation for residual glasses, Pl, Cpx, and Fe oxides. Please refer to the text for details.

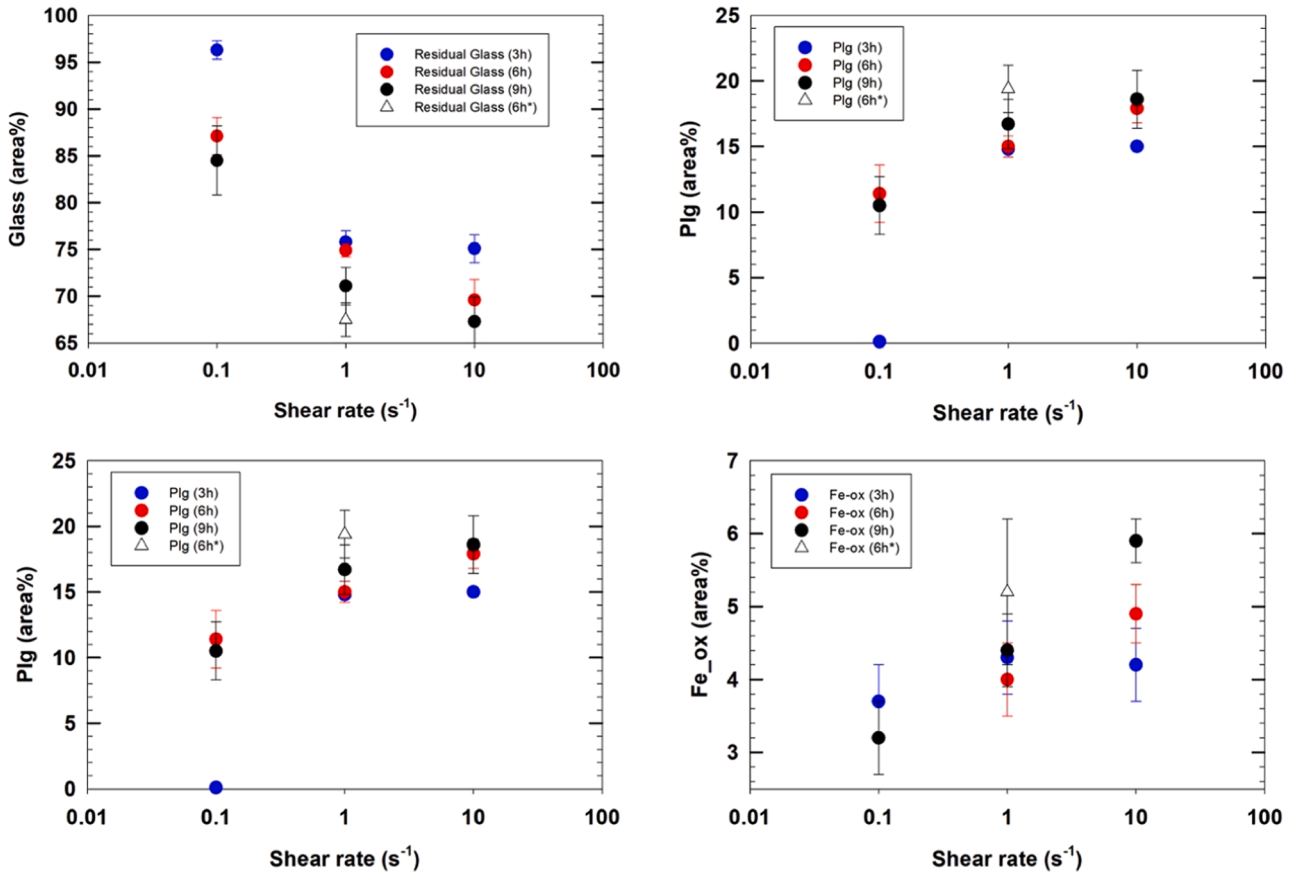

Fig. 4. Note: Residual glasses (A), Plg (B), Cpx (C) and Fe-Ox (D) as derived from image analysis results. For details, please refer to text and Table 3. The white triangle refers to the SR1 s^{-1} run suffering thermal cycling.

Table 3
Maximum and average growth rates and appearance of solid phases.

run#	Solid phases	$\frac{G_{max}}{G_{av.}}$ cm/s	run#	Solid phases	$\frac{G_{max}}{G_{av.}}$ cm/s	run#	Solid phases	$\frac{G_{max}}{G_{av.}}$ cm/s	run#	Solid phases	$\frac{G_{max}}{G_{av.}}$ cm/s
SR0 3h	Ox	5.82E-07 1.18E-07	**SR0.1 3h**	Ox	4.60E-07 1.25E-07	**SR 1 3h**	Ox	4.31E-07 7.95E-08	**SR 10 3h**	Ox	3.44E-07 8.35E-08
							Plg	2.14E-06 2.46E-07		Plg	1.11E-06 1.86E-07
							Cpx	4.45E-07 7.65E-08		Cpx	3.16E-07 7.01E-08
						SR 1 6h*	*Ox*	*1.64E-07* *3.52E-08*			
							Plg	*1.06E-06* *2.38E-07*			
							Cpx	*3.38E-07* *8.10E-08*			
SR0 6h	Ox	3.87E-07 6.37E-08	**SR0.1 6h**	Ox	3.15E-07 3.36E-08	**SR 1 6h**	Ox	2.00E-07 1.76E-08	**SR 10 6h**	Ox	1.57E-07 2.80E-08
				Plg	9.49E-07 1.27E-07		Plg	7.27E-07 1.14E-07		Plg	6.23E-07 8.76E-08
				Cpx	1.46E-07[£] 1.23E-07[£]		Cpx	1.98E-07 2.90E-08		Cpx	1.63E-07 2.22E-08
SR0 9h	Ox	1.47E-07 5.94E-08	**SR0.1 9h**	Ox	3.77E-07 2.71E-08	**SR 1 9h**	Ox	2.10E-07 1.95E-08	**SR 10 9h**	Ox	1.49E-07 2.46E-08
				Plg	7.91E-07 1.40E-07		Plg	5.66E-07 1.03E-07		Plg	3.13E-07 5.13E-08
				Cpx	1.58E-07 5.00E-08		Cpx	1.62E-07 3.21E-08		Cpx	1.28E-07 2.31E-08

Note: solid phases appearance depending on time and shear rate applied. Growth rates are reported as maximum and average growth rate (G_{max} and G_{av}, respectively). For details refer to the main text. Run SR 1 6h* in italics refers to the "failed" experiments where temperature cycling happen.
[£] very few crystals analyzed (please refer to Table 3).

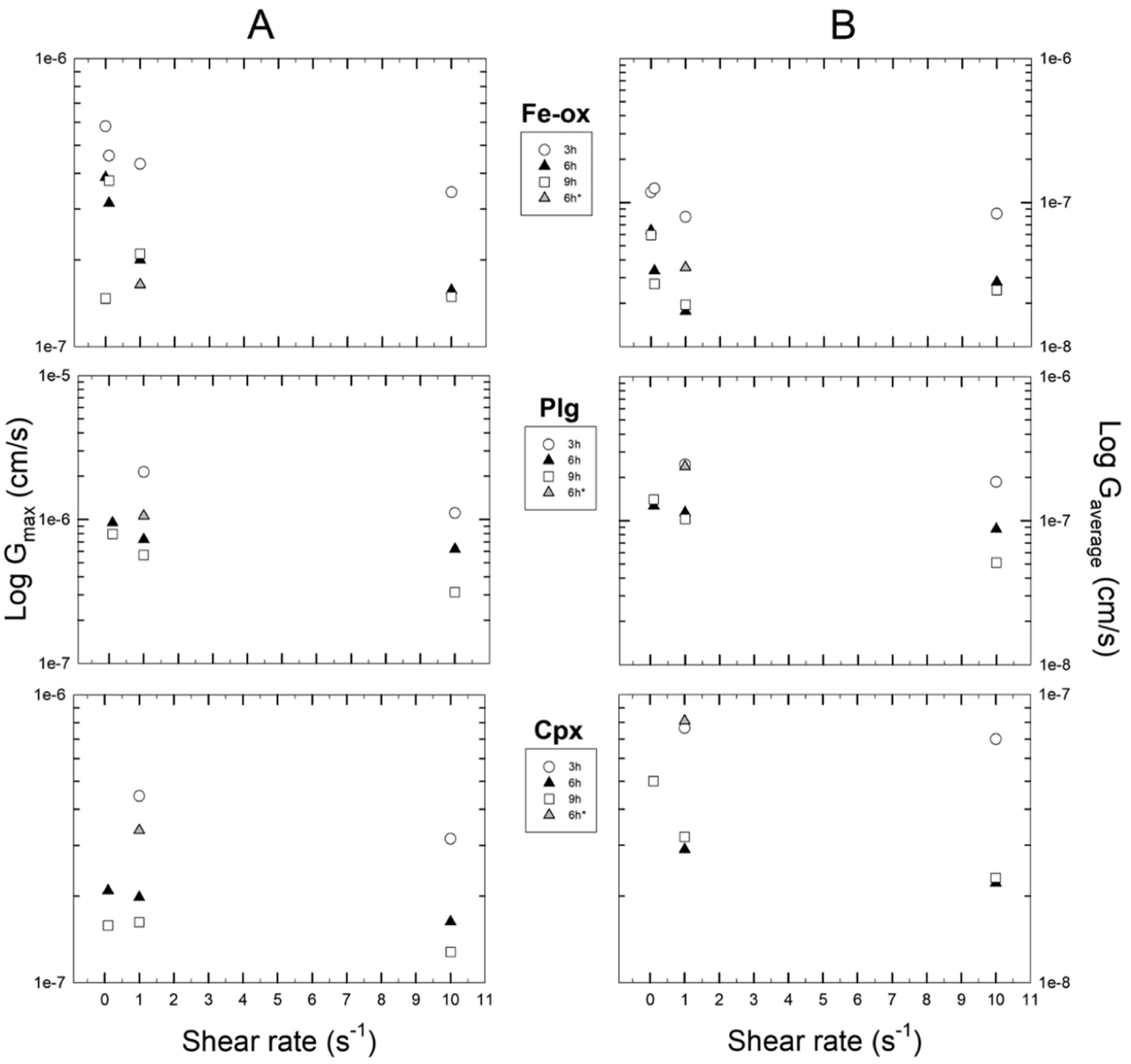

Fig. 5. Maximum (left diagrams; A) and average (right diagrams; B) growth rates for Fe-ox, Plg and Cpx as a function of the applied shear rate and time.

+ 1 deformation-bearing runs plus deformation-free runs where only Fe-oxides nucleate and grow. In the following, the run-product suffering thermal cycling will be not more considered

3.4. Rheology of partially crystallized basalt

All the experiments were monitored to track the viscosity evolution over time at the different shear rates applied and at 1150 °C. Fig. 6**A** reports the evolution of viscosity, in log Pa s, for shear rates of 0.1, 1 and 10 s^{-1}, respectively. The maximum measured viscosity is 2.90, 3.83 and 4.89 log (Pa s) as $\dot{\gamma}$ decreases from 10 to 1 and finally 0.1 s^{-1}. As will be explained in the discussion and visible in Fig. 6, after certain time (depending on the applied shear rate), there is a drop in viscosity and an increasing noise on data that is related to the partial or total detaching of the spindle from the sample (ductile-fragile transition).

The main outcome from the viscosity paths is first a clear increase in viscosity (from time 0 on) followed by an abrupt decrease after ~ 45, ~ 180 and ~ 380 min as the shear rate goes from 10 to 1 and 0.1 s^{-1}, respectively.

This behaviour is highlighted in Fig. 6**B, C and D** respectively, where the arrows indicate the point at which viscosity starts to drop for samples SR 10–9 h, SR 1–9 h, SR 0.1–9 h. Fig. 6 show the viscosity evolution for 9 h experimental runs. Viscosity data from the other 3 and 6 h runs perfectly overlap the first part of the 9 h curve presented in Fig. 6, proving the reliability of the reproducibility of the applied technique for viscosity determinations.

4. Discussion

4.1. Effect of shear rate on crystal chemistry

The EPMA data for all the investigated samples are provided as supplementary material (Table S1, S2–1, S2–2 and S3 and related Figures S2, S3 and S4). We do not observe significant changes for Plg composition as both time and shear rate vary being all these crystals close to An_{68}. Conversely, all the measured Cpx show variability as clearly captured by CaO vs FeOt plots reported in supplementary material **Figure S6** and Table S2. There is clearly a chemical dichotomy, allowing sector zoning to develop in individual crystals. This results in two populations that we labelled “bright” and dark” Cpx. The dark Cpx

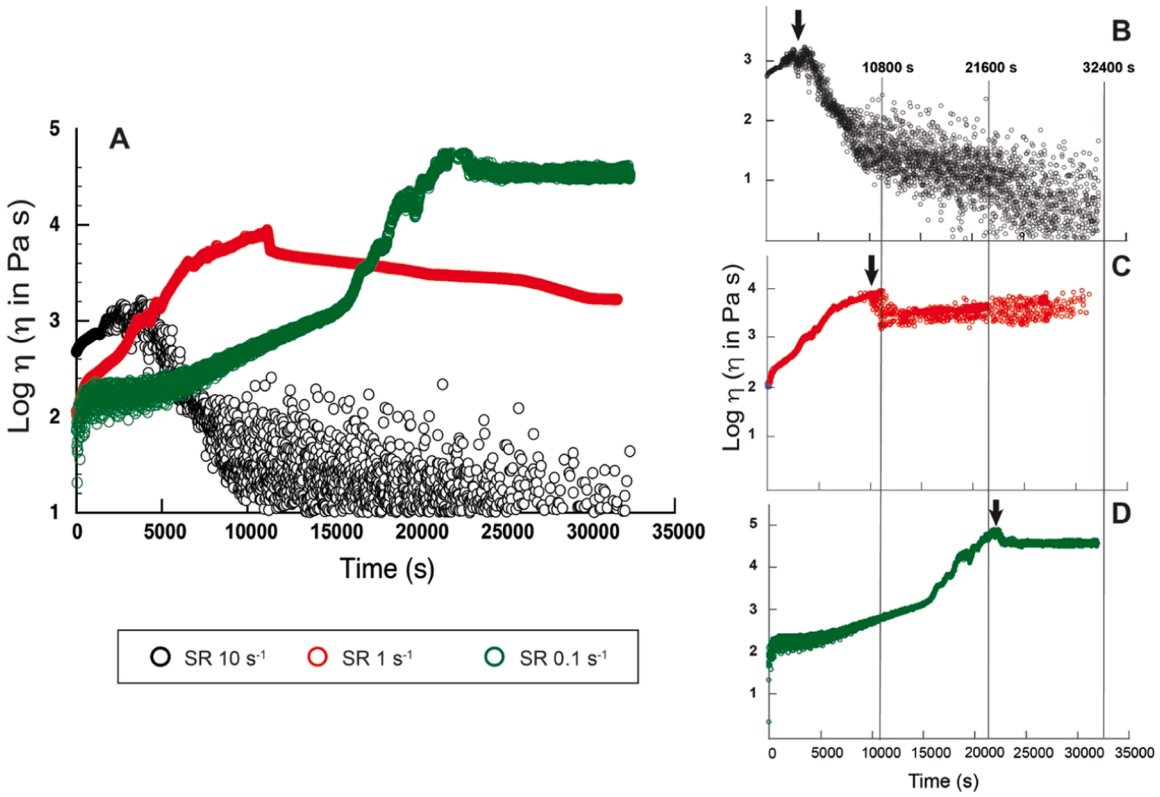

Fig. 6. Log viscosity (Pa s) vs time for the three shear rate investigated after 9 h run (A). The right part show log viscosity (Pa s) vs time for experimental runs at 1150 °C and $\dot{\gamma} = 10\ s^{-1}$ (B), $1\ s^{-1}$ (C) and finally, $0.1\ s^{-1}$ (D). Black arrows in run at $\dot{\gamma} = 10\ s^{-1}$ (B), indicate the brittle-fragile transition with a drop in viscosity due to the detachments of partially crystallized melts showing shear stress = 7244 Pa. Arrows for $\dot{\gamma} = 1$ and $0.1\ s^{-1}$ runs (C and D, respectively) also show a drop in viscosity, but the detachments were not clearly visible after quenching with a maximum shear stress close to 7.000 Pa.

usually has high silica and relatively low FeO content compared to the bright Cpx. If we consider time only and fix the shear rate, we can observe a progressive shift toward lower FeO and CaO as time increases for both 0.1 and $1\ s^{-1}$ runs (Figure S6 A and C).

As the shear rate reaches $10\ s^{-1}$, the Cpx always shows some chemical variability, but it seems that the bright Cpx is more homogeneous when compared to the dark Cpx. On the other hand, for 3 h runs, Cpx shows a chemical shift to high FeO and CaO at a lower shear rate (Figure S6 B) and this trend is similar for 6 h runs (Figure S6 D). However, the Cpx of 9 h runs show a more defined cluster, possibly due to the higher crystallinity throughout the samples. The sector zoning patterns of Cpx crystals representative of different run durations and shear rates are highlighted on BSE images in **Figure S7**.

Sector zoning results from compositional differences among adjacent crystal regions that grow simultaneously (Mollo et al., 2023). We compared the major element composition of Cpx of the two different sector zoning populations using molecular attributes: the sum of diopside (Di; $CaMgSi_2O_6$) and hedenbergite (Hd; $CaFeSi_2O_6$) components vs the sum of Ca-Tschermak (CaTs; $CaAl_2SiO_6$) and CaTi-Tschermak (CaTiTs; $CaTiAl_2O_6$) components. Being aware that changes in Cpx components are the window to depict the different proportions of $^{T}Si + {}^{M1}Mg$ and $^{T}Al + {}^{M1}Ti$ cations in the different zoning patterns, we have used these Cpx components as tracer for Cpx evolution through time and shear rate. As already shown by Mollo et al. (2023), we confirm that sector zoning mirrors the enrichment and depletion criteria $[Di + Hd]_{\{-1\ 1\ 1\}} > [Di + Hd]_{\{h\ k\ 0\}}$ and $[CaTs + CaTiTs]_{\{-1\ 1\ 1\}} < [CaTs + CaTiTs]_{\{h\ k\ 0\}}$, although the data of Mollo et al. (2023) were obtained at different pressure and temperature conditions and from decompression experiments. As a whole, crystal compositions from experiments SR0.1–9 h vs SR0.1–6 h and SR1–9 h vs SR1–6 h and SR1–3 h are preferentially enriched in $[Di + Hd]_{\{Dark\ Cpx\}}$ in concert with lower proportions of $[CaTs + CaTiTs]_{\{Dark\ Cpx\}}$ components, whereas those obtained at higher shear rate and 3, 6 and 9 h do not show a clear trend, although a slightly progressive shifting (positive correlation of $[CaTs + CaTiTs]_{\{Dark\ Cpx\}}$ vs $[Di + Hd]_{\{Dark\ Cpx\}}$ toward high $[CaTs + CaTiTs]_{\{Dark\ Cpx\}}$ as time increases can be observed. The role of the shear rate is more difficult to be resolved by using Cpx component (Fig. 7).

The relationship between $[CaTs + CaTiTs]_{\{Bright\ Cpx\}}$ vs $[Di + Hd]_{\{Bright\ Cpx\}}$ presented in Fig. 7 mirrors, as a whole, those presented for the dark Cpx and compositional differences between different experiments are more evident if data obtained at constant shear rate are compared with each other (Figure S6). However, the highest applied shear rate seems to reduce both the compositional range of $[Di + Hd]_{\{Bright\ Cpx\}}$ and of $[CaTs + CaTiTs]_{\{Bright\ Cpx\}}$ (variations of 0.55 ± 0.05 and 0.17 ± 0.1, respectively, Fig. 7C). This final point propels systems towards compositional equilibrium with remarkable celerity compared to their slowly stirred counterparts. In synthesis, the increasing of solidification time and to a lesser extent the shear rate both favor the stabilization of the Di- and Hd-rich (*equilibrium*) molecules at the expense of Tschermak ones (Fig. 7).

4.2. *Effect of shear rate on solid phase appearance and related growth rate*

The composition of silicate liquid influences the time needed for crystals to nucleate and grow (Vetere et al., 2015; Rusieka et al., 2020). It has a central role in understanding magma behaviours, especially during their ascent and prior to their eruption (Marsh, 1988a,b; Costa et al., 2008; Cooper, 2017 and K.M. 2019; Putirka, 2017; Polacci et al., 2018). The viscosity of any magma suspension is controlled by solid phases, thus a function of their nucleation and growth behaviours, as well as on the temperature below the liquidus temperature at which

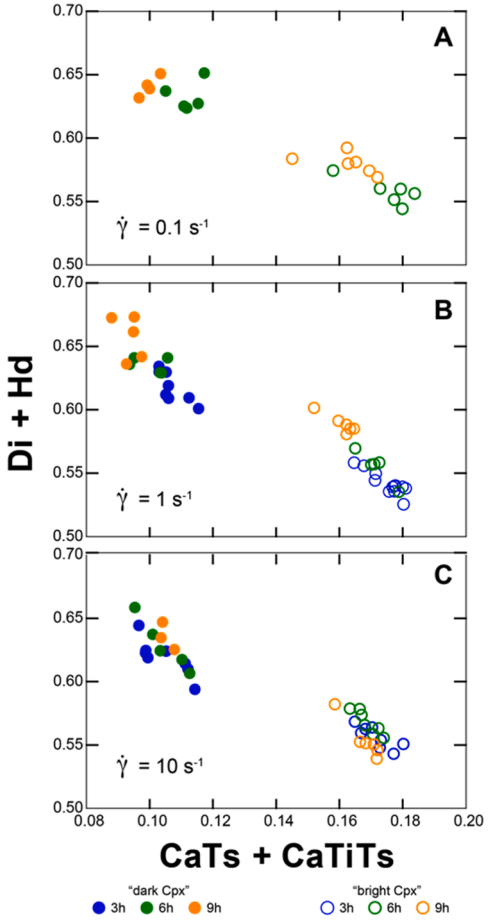

Fig. 7. Clinopyroxene components from the dynamic runs, determined from microprobe data, following the calculation scheme described in Mollo et al. (2018). CaTs, Ca-Tschermak. CaTiTs, CaTi-Tschermak. Di, diopside. Hd, hedenbergite.

magma is subjected, i.e. the undercooling degree (e.g., Vona and Romano, 2013; Tripoli, 2019; Rusiecka et al., 2020: Vetere et al., 2021; Mollo et al., 2022; Di Fiore et al., 2023). Tripoli et al. (2019) studied the effects of shear rate on crystallization kinetics of basaltic magma. Measurements were performed at subliquidus conditions (1160 °C, i.e. 10° higher than the experimental temperature proposed in this study) by applying strain rates from 0 to $2 \times 10^{-4}\ s^{-1}$. During the experiment, the sample was analyzed with X-ray micro-tomography. They highlighted that crystallization of oxides did not occur in deformation-free runs. However, first crystallization occurred after starting the sample deformation, proving that the increase of the strain rate enhances both the nucleation rate and of the crystal growth rate, and, also, a decrease of the incubation time (time needed for a system to nucleate and finally growth crystals). These observations of Tripoli et al. (2019) made for oxides agree with the 3 runs at zero (deformation-free) performed here (1400 °C for 2 h and then cooling to 1150 °C). Our results confirm that the findings of Tripoli et al. (2019) also apply to silicate minerals and that the delay time for nucleation also depends on the shear rate. This was further confirmed by Vetere et al. (2021) on an andesitic composition (Calbuco volcano, Chile). Moreover, the observed increase of the effective viscosity after a so-called delay time (δ_t; Rusiecka et al. 2020) was a prove of the impact of nucleation and growth of solid phases in the investigated system.

Therefore, in line with previous investigations and the outcomes reported above it is evident that deformation affects the crystallization kinetics of magmas, i.e., activation energy and diffusion process governing nucleation and crystal growth. In this study, further constraints on the incubation time (delay time) for Plg are provided, showing that it first appears after 3 h in the experimental run at 0.1 s^{-1} and 1150 °C, (as above specified, only 1 plagioclase was detected after 3 h run); this duration can be considered as the Plg delay time for its nucleation, while for Cpx we have to consider a minimum incubation time that is between 3 and 6 h (Fig. 1 and Tables 2 and 3). In contrast to silicates, Fe-oxides are <3 h, thus extremely rapid and at the lowest undercooling degree than Plg and Cpx (at~ 1150 °C and same shear rate; Tripoli et al., 2019). As proposed by Vona et al. (2011 and 2013) the evolution of viscosity could track the appearance of solid phases, at least when their sizes and amount are enough to influence the rheological attributes. By looking at the viscosity data presented in Fig. 6 they appear to be scattered and difficult to interpret at the beginning of the experiment at 0.1 s^{-1}. Qualitatively, it seems that viscosity starts to increase after at least 1 h (Fig. 6D). By increasing the shear rate to 1 s^{-1}, all the phases are present after 3 h and we do not have any quantitative indication for the delay time. If viscosity data are considered, it appears that delay time is almost negligible since the viscosity increase for a shear rate of 1 and 10 s^{-1} is immediate. In other words, deformation is a key factor for phases to nucleate and grow, and faster deformation rates allow the almost immediate appearance of silicate phases at the condition investigated here. The faster crystal growth that is related to the shear rate implies that shearing is feeding the crystal for fast growth because it increases the elements mobility towards the crystal-melt interface.

Frequently, among the different methods applied for determining crystal growth rates (G), scientists measure the crystal length (L) divided by experimental time (Cashman, 1993; Pupier et al., 2008; Brugger and Hammer, 2010; Shea and Hammer, 2013; Cooper and Kent, 2014; Arzilli et al., 2016; Mollo and Hammer, 2017). In these studies, performed at deformation-free conditions, the estimated growth rates are given as constant values. However, in our experiments we note that for the silicate phases, the growth rate varies as a function of the shear rate but also over the experimental duration (at constant shear rate). On average, deformation-free runs show the faster growth rate for Fe-oxides and this possibly relies on the fact that they are the only phase growing at these conditions without any interferences due to the appearance of other solid phases as the shear rate increases. Moreover, it can also be hypothesized that at these conditions, the initial nucleation rate of Fe-oxides is lower than at 0.1, 1 and 10 s^{-1}, favoring the growth of a more limited number of crystals but with larger sizes than at deformation-bearing conditions. A third concomitant effect could be the absence of agglomeration or coalescence at zero shear, differently from deformation-bearing experiments; this also can affect the *ex-situ* measurements of growth rates (Giuliani et al., 2020).

For the Fe-oxides after 3, 6 and 9 h, at no shear, we calculate the highest growth rate (5.82×10^{-7} cm/s) after 3 h and applying the lowest shear rate, their growth rate first reaches 4.60×10^{-7} cm/s and then, as time proceed to 6 and 9 h, respectively, G_{max} decreases to approximately identical values of 1 to 2×10^{-7} cm/s (Table 3 and Fig. 5). This trend is similar for the experiments performed at 1 and 10 s^{-1}, having an almost exponential decrease as the shear rate increases. An identical trend is also observed when G_{av} is considered. Moreover, Fig. 5 shows that the longer the experimental time, the lower the G values. Plagioclase appears at the end of the 3 h experiment at the lowest shear rate (a single small crystal found in all the 1914 BSEs images investigated) and the growth rate in this run was not taken into account. For all the other runs, experimental results suggest that there is strong variability showing the highest growth rate at the highest shear rate (run SR10–3 h, 10 s^{-1}, 1.11×10^{-6} cm/s). Similar results were found for run SR10–3 h at 1 s^{-1} with a calculated growth rate of 1.23×10^{-6} cm/s (Table 2). Cpx is the last phase to appear with the higher growth rates estimated at the shear rate 1 and 10 s^{-1} and after a 3 h run (samples SR1–3 h and SR10–3 h; 4.45–3.16 $\times 10^{-7}$ cm/s; Table 3). We can argue that those results rely on the complex interplay between shear rate and element mobility. The latter decreases with time due to changes in residual liquid rheology (becoming more viscous over time, see residual melts evolution in

Table 1 and Fig. 2).

The plagioclase growth rate values calculated above are significantly larger than those obtained at static conditions (i.e., 10^{-8}–10^{-9} cm/s; Pupier et al., 2008) and closer to those proposed by Vona and Romano (2013) and Chevrel et al. (2015) and Vetere et al. (2021) in the limit of chemical differences of these basaltic starting materials. The starting materials used by Vona and Romano (2013; basalts from Etna and Stromboli volcanoes) are much closer to our composition and it is interesting to compare their results in terms of plagioclase growth rate. Stromboli plagioclase average growth rates display a relatively small variation with undercooling (1.9–3.4 $\times$ 10^{-7} cm/s) while Etna data indicate $G = 0.6–1.9 \times 10^{-7}$ cm/s (note that Vona and Romano, 2013, used a different approach to calculate G; see their Eq. 4 were $G = \left[(l \times w)^{0.5}\right]/[2 \times \Delta T]$ and the shear rate continuously changes and decreases as the maximum torque is achieved; in our case, the shear rate is always constant until reaching a critical point, please refer to paragraph 4.3).

Comparison with growth rates in similar magmatic systems was also proposed recently by Giuliani et al. (2020). Although the experimental strategy was very different (continuous cooling rate applied to the basaltic system), it is interesting to note that both spinel and Cpx growth rates are similar to those presented here at a rate of cooling close to 7 °C/h. Vetere et al. (2021) investigated the plagioclase growth rate imposing a shear rate of 0.5 s^{-1} and 1210 °C in a basaltic andesite system and have proposed G_{max} values between 1.45 $\times$ 10^{-6} and 9.71 $\times$ 10^{-7} cm/s. Those values agree with values calculated here for plagioclase in Etna magma, although the shear rates investigated is much wider. Perhaps the most intriguing result relies on the crystal growth change with time. Independently if one considers G_{av} or G_{max} values for any phases presented in Table 3 and Fig. 5, it appears that the fastest rate relies on the short experimental time. While the mean G value understandably declines with increasing experimental duration, we contend that the true G exhibits temporal variability in a non-linear manner. Under identical conditions but with extended experimental time, one would anticipate comparable growth rates for the crystals, provided simultaneous nucleation and growth events. For example, assuming a constant growth rate, the crystallization of a hypothetical phase "z" would manifest a G1 magnitude in the initial 3-hour experiment. However, following a 6-hour experiment (maintaining constant parameters such as temperature, pressure, oxygen fugacity, and starting compositions), it would transition to a lower G2 value.

This changing growth rate may be related to the evolution of crystal size (and consequently of the surface in contact with the silicate melt) with time. This point is extremely important in assessing the growth rate in magmatic systems; identical melts undergoing partially crystallizing events could show very different growth rates of crystals strictly dependent on the size and specific surface area of the minerals. Crystals aspect ratio shows elongated Plg (some Plg have AS > 20 and on average 4.0<AS>4.9 as shown in supplementary material Figures S5). Since crystal growth has to cope with crystal abundance, it appears that the higher the volume of solid phases, the lower the chance for crystal to increase their size. Nevertheless, considering that plagioclase growing in experiments SR10–9 h at highest shear rate has the support of spindle rotation (e.g. high element mobility) for only 45 min before brittle-fragile transition occurs, it appears evident magma dynamics has a high impact on crystals nucleation and growth.

Moreover, considering experiments SR1–6 h and SR1–6h* in Fig. 1, the two samples conducted with and without thermal cycling, they show not only different AS (more elongated Plg for sample SR16h*; Figure S5.2 A and B), but also different plagioclase sizes (bigger for sample SR16h*; Figure 5.2 C) and area% (see Table 2), pointing to the important role of thermal fluctuations and shearing in magmas.

4.3. Rheological behaviour of basalt and ductile-fragile transition

As shown in Fig. 6, the viscosity increases as the shear rate decreases and this points to possible shear thinning behaviour for the investigated system. This behaviour is well-known for mafic systems in the literature and a comprehensive review was proposed by Vetere et al. (2022) reporting the variation in viscosity at identical crystal content for different magmatic systems (see Fig. 7 in Vetere et al., 2022). Here, the apparent viscosity (viscosity measured at certain $\dot{\gamma}$ and temperature) does not reach the classical plateau as reported in the literature (Vona et al., 2013), where, after a certain delay, viscosity increases along a sigmoidal path (viscosity vs time) and finally reaching a plateau of constant viscosity where crystallization processes end.

Complex variation in the apparent viscosity, pointing to non-equilibrium rheology is still an unexplored field of investigation. All the 3 experimental runs at 10 s^{-1} clearly showed, after the quenching, a rupture between the part of the material sticking to the spindle and the rest of the material into the crucible. This is clear evidence that the ductile-fragile transition is reached as the shear stress reaches a value of ~ 7200 Pa. This behaviour was not clearly observed for experimental runs at lower shear rates of 1 s^{-1} and 0.1 s^{-1}. In particular, those experiments showed surface initial rupture at slightly lower shear stress values, indicating a possible ductile-fragile transition close to 7000 Pa. Our conclusion points to a ductile-fragile transition when the Etna Basalt reaches shear stress > 7000 Pa at the investigated conditions. This transition point is highlighted by the black arrows in Fig. 6, indicating a drop in viscosity in the time-dependent measurements (Fig. 6B-D).

4.4. Implication for magma dynamics

Our data can have profound implications on the rheological behaviours of magmas. In particular, viscosity is highly influenced by the amount and textures of solid phases, which allows magmas or lavas to continue their ascent along conduits and dikes or stop within the crust or lavas to flow on Earth's surface.

After a certain time and depending on the applied shear rate, the effective viscosity measured suffers a sudden change (Fig. 6), confirming what was highlighted by F. Vetere et al. (2019). They studied the viscosity evolution from superliquidus to subliquidus conditions, applying 10 °C/hr cooling rate for a pyroxenite melt; they reported a detachment between a part of the sample stacked on the spindle and the sample into the crucible and proposed a brittle failure of the system when viscosity reached the value of approximately of 4.77 log (Pa·s) at 1195 °C. The highest viscosity measured here (approximately 6.0 $\times$ 10^4 Pa·s) at a shear stress of 5960 Pa possibly corresponds to the brittle failure in the pyroxenite system. Although F. Vetere et al. (2019) presented experimental viscosity data under cooling conditions, it is interesting to note that by applying an identical shear rate (0.1 s^{-1}), the anomalous viscosity data reading (Fig. 7 in F. Vetere et al. 2019; caused by a circular fracture of the melt + crystal system) corresponds to the ones observed here at isothermal conditions. Interestingly, the time interval before detachment occurs almost identical to what we measured in this study (close to 22000s; Fig. 6). Finally, the ductile-fragile transition of the system investigated by F. Vetere et al. (2019) occurred when viscosity reached the value of approximately 4.77 log (Pa·s) at 1195 °C at a shear stress of 5960 Pa. These threshold values are 4.89 log (Pa·s) at 1150 °C at a shear stress of 7200 Pa, respectively. Considering that the starting materials are quite different (pyroxenite vs basalt), it seems that the ductile fragile threshold tends to increase as the system becomes SiO_2 richer. This qualitative consideration deserves a more focused and systematic experimental approach to be confirmed.

In summary, the more rapid change in rheological behaviour at higher strain rates and suppression of vitrification. This can be mainly ascribed to two cooperative processes enhanced by the presence of deformation: a) the dynamics of the system that can efficiently enhance crystal nucleation (increasing of nucleation rate), as also suggested in

literature (Cashman et al., 1999; Emerson, 1926; Vona and Romano, 2013) and b) a continuous feeding of the individual crystal surfaces by "fresh ingredient" that could facilitate the crystal growth as shown, for example, in the simulation of magmatic conditions (Petrelli et al., 2016). The new and large deformation-free and deformation-bearing experimental solidification run-products reported here straightforward point out that a progressive increase in shear rate induces a rapid and vigorous crystallization (Fig. 4); this leads to an earlier ductile fragile transition that could promote either a) highly energetic eruption by promoting fragmentation or b) the stalling of ascending magmas.

5. Conclusions

The (*ex-situ*) crystallization and (*in-situ*) rheological paths of a basaltic silicate liquid cooled from *superliquidus* to moderate *subliquidus* conditions (1150 °C and ΔT of ~ 40 °C, quenched after 3, 6 and 9 h) under deformation-free (0 s^{-1}) and -bearing (0.1, 1 and 10 s^{-1}) regimes are markedly variable. At zero shear, only Fe-oxides nucleate, whereas silicate phases require the presence of a shear rate; except for Plg at 0.1 s^{-1}, both Cpx and Plg crystallize in a time lesser than 3 h. The presence and magnitude of deformation also affect the crystal-chemistry of Cpx. For basaltic anhydrous systems, the measured growth rate is much larger (e.g. Plg goes up to 10^{-6} cm/s) than values provided by literature for deformation-free conditions (10^{-8}–10^{-9} cm/s). Thus, the growth rate can change by 2–3 orders of magnitude in the case of deformation-bearing systems, which could completely change the rheology of magmas, the ascent of magmatic suspensions in dikes and conduits, the eruptive behaviours and the lava flow emplacements. Also, changes induced by different shear rates have a direct impact on the apparent viscosity values that are inversely related to the applied shear rate: the higher the shear rate the lower the apparent viscosity (shear thinning behaviour). Finally, this study evidences that possible ductile-fragile transition for the Etna basalt at 1150 °C is observable as the shear stress is higher than 7000 Pa. The results attained here reduce the gaps between real solidification conditions occurring in the natural domain and simulations performed in the laboratory by clarifying the key role of deformation on nucleation, crystal growth and rheology. These outcomes contribute to better building a theoretical base for general models aimed at predicting magmatic and volcanic dynamics.

CRediT authorship contribution statement

Francesco Vetere: Writing – review & editing, Writing – original draft, Validation, Methodology, Funding acquisition, Data curation, Conceptualization. **Sven Merseburger:** Writing – review & editing, Methodology, Data curation. **Alessandro Pisello:** Methodology, Formal analysis, Data curation. **Diego Perugini:** Writing – review & editing, Conceptualization. **Cecilia Viti:** Writing – review & editing, Methodology, Conceptualization. **Maurizio Petrelli:** Writing – review & editing, Data curation. **Alessandro Musu:** Methodology, Formal analysis. **Renat Almeev:** Data curation. **Luca Caricchi:** Writing – review & editing, Data curation. **Gianluca Iezzi:** Writing – review & editing, Conceptualization. **Michele Cassetta:** Data curation. **Francois Holtz:** Writing – review & editing, Conceptualization.

Declaration of competing interest

The authors declare that they have no known competing financial interests or personal relationships that could have appeared to influence the work reported in this paper.

Data availability

Data will be made available on request.

Acknowledgements

This study was funded by the "Piano di Sostegno alla Ricerca 2022 per finanziamenti a progetti di ricerca Curiosity-driven (UniSi, F-CUR CREAMI)" awarded to F.Vetere. This study was also funded by the PRIN (2009PZ47NA_003) project "Time Scales of Solidification in Magmas: Application to Volcanic Eruptions, Silicate Melts, Glasses, Glass-Ceramics" and the "Fondi Ateneo of the University G. D'Annunzio" awarded to G. Iezzi. The analytical work benefited from the microprobe financed by DFG proposal INST 187/737–1 FUGG to Leibniz University Hannover. D. Perugini and M. Petrelli acknowledge the PRIN (202037YPCZ_001) project "Dynamics and timescales of volcanic plumbing systems: a multidisciplinary approach to a multifaceted problem". University of Perugia, Fondi di Ricerca di Ateneo2021, WP3.1 "Disastri e Crisi Complesse" Project "Studio di scenari multirischio per i disastri naturali nell'area dell'Italia centro-meridionale e della Sicilia: capire il passato e il presente per proteggere il futuro" is also acknowledged. D. Perugini and M. Petrelli acknowledge the support from MUR in the framework of SUPER-C, 'Dipartimento di Eccellenza 2023–2027'

Supplementary materials

Supplementary material associated with this article can be found, in the online version, at doi:10.1016/j.epsl.2024.118934.

References

Andronico, D., Branca, S., Calvari, S., et al., 2005. A multi-disciplinary study of the 2002–03 Etna eruption: insights into a complex plumbing system. Bull. Volcanol. 67, 314–330. https://doi.org/10.1007/s00445-004-0372-8.

Arzilli, F., La Spina, G., Burton, M.R., Polacci, M., Le Gall, N., Hartley, M.E., et al., 2019. Magma fragmentation in highly explosive basaltic eruptions induced by rapid crystallization. Nat. Geosci. 12, 1023–1028.

Arzilli, F., Piochi, M., Mormone, A., Agostini, C., Carroll, M.R., 2016. Constraining pre-eruptive magma conditions and unrest timescales during the Monte Nuovo eruption (1538 AD; Campi Flegrei, Southern Italy): integrating textural and CSD results from experimental and natural trachy-phonolites. Bull. Volcanol. 78, 72. https://doi.org/10.1007/s00445-016-1062-z.

Behncke, B., Neri, M., 2003. Cycles and trends in the recent eruptive behaviour of Mount Etna (Italy). Can. J. Earth Sci. 40, 1405–1411. NRC Research Press Ottawa, Canada.

Branca, S., Carlo, P.D., 2005. Types of eruptions of Etna volcano AD 1670–2003: implications for short-term eruptive behaviour. Bull. Volcanol. 67, 732–742. Springer.

Branca, S., Coltelli, M., Groppelli, G., 2004. Geological evolution of Etna volcano. Washington DC Am. Geophys. Union Geophys. Monograph Series 143, 49–63.

Brugger, C.R., Hammer, J.E., 2010. Crystal size distribution analysis of plagioclase in experimentally decompressed hydrous rhyodacite magma. Earth. Planet. Sci. Lett. 300, 246–254. https://doi.org/10.1016/j.epsl.2010.09.046.

Cappello, A., Bilotta, G., Neri, M., Negro, C.D., 2013. Probabilistic modeling of future volcanic eruptions at Mount Etna. J. Geophys. Res.: Solid Earth 118, 1925–1935. Wiley Online Library.

Cashman, K., Thornber, C., Kauahikaua, J., 1999. Cooling and crystallization of lava in open channels, and the transition of Pahoehoe Lava to 'A'(a)over-bar. Bull. Volcanol. 61, 306–323. https://doi.org/10.1007/s004450050299.

Cashman, K.V., 1993. Relationship between plagioclase crystallization and cooling rate in basaltic melts. Contrib. Mineral. Petrol. 113 (1), 126–142. https://doi.org/10.1007/BF00320836.

Cashman, K.V., Soule, S., Mackey, B., Deligne, N., Deardorff, N., Dietterich, H., 2013. How lava flows: new insights from applications of lidar technologies to lava flow studies. Geosphere 9 (6), 1664–1680. https://doi.org/10.1130/GES00706.1.

Chevrel, M.O., Cimarelli, C., deBiasi, L., Hanson, J.B., Lavallée, Y., Arzilli, F., Dingwell, D.B., 2015. Viscosity measurements of crystallizing andesite from Tungurahua volcano (Ecuador). Geochem. Geophys. Geosyst. https://doi.org/10.1002/2014GC005661.

Cooper, K.M., 2017. What does a magma reservoir look like? The "crystal's - eye" view. Elements 13, 23–28. https://doi.org/10.2113/gselements.13.1.23.

Cooper, K.M., Kent, A.J.R., 2014. Rapid remobilization of magmatic crystal kept in cold storage. Nature 506. https://doi.org/10.1038/nature12991.

Cooper, K.M., 2019. Time scales and temperatures of crystal storage in magma reservoirs: implications for magma reservoir dynamics. Phil. Trans. R. Soc. A 377, 20180009. https://doi.org/10.1098/rsta.2018.0009.

Corsaro, R.A., Miraglia, L., 2022. Near real-time petrologic monitoring on volcanic glass to infer magmatic processes during the February–April 2021 paroxysms of the south-east crater, etna. Frontiers in Earth Sci. 10.

Costa, F., Dohmen, R., Chakraborty, S., 2008. Time Scales of magmatic processes from modeling the zoning patterns of crystals. In: Putirka, K.D., Tepley, F.J. (Eds.), Rev. Mineral., 69, pp. 545–594. https://doi.org/10.2138/rmg.2008.69.14.

Couch, S., 2003. Experimental investigation of crystallization kinetics in a haplogranite system. Am. Mineral. 88, 1471–1485.
Di Fiore, F., Vona, A., Mollo, S., et al., 2023. Experimental insights on the shear-induced crystallization of a phonotephrite magma. Chem. Geol. 637, 121682, 2023.
Dingwell, D.B., 1991. Redox viscometry of some Fe-bearing silicate melts. Am. Mineral. 76, 1560–1562.
Dingwell, D.B., Virgo, D., 1988. Viscosity oxidation state relationship for hedenbergitic melt. Carnegie Inst. Wash. Yearbook 87, 48–53.
Emerson, O.H., 1926. The formation of aa and pahoehoe. Am. J. Sci. 68, 109–114.
Erdmann, M., Koepke, J., 2016. Silica-rich lavas in the oceanic crust: experimental evidence for fractional crystallization un- der low water activity. Contrib. Mineral. Petrol. 171, 83. https://doi.org/10.1007/s00410-016-1294-0.
Giuliani, L., Iezzi, G., Vetere, F., Behrens, H., Mollo, S., Cauti, F., Ventura, G., Scarlato, P., 2020. Evolution of textures, crystal size distributions and growth rates of plagioclase, clinopyroxene and spinel solidified at variable cooling rates from a mid-ocean ridge basaltic liquid. Earth Sci. Rev. 204, 103165.
Hammer, J.E., Rutherford, M.J., 2002. An experimental study of the kinetics of decompression-induced crystallization in silicic melt. J. Geophys. Res. 107 (B1), 2021. https://doi.org/10.1029/2001JB000281.
Iezzi, G., Mollo, S., Torresi, G., Ventura, G., Cavallo, A., Scarlato, P., 2011. Experimental solidification of an andesitic melt by cooling. Chem. Geol. 283, 261–273.
Iezzi, G., Mollo, S., Ventura, G., Cavallo, A., Romano, C., 2008. Experimental solidification of anhydrous latitic and trachytic melts at different cooling rates: the role of nucleation kinetics. Chem. Geol. 253, 91–101.
Kerr, R.C., Lister, J.R., 1991. The effects of shape on crystal settling and on the rheology of magmas. J. Geol. 99, 457–467.
Klöß, G.H., 2000. Dichtefluktuationen Natürlicher Gläser. Habilitation thesis. Universtiy of Jena (in German).
Kolzenburg, S., Giordano, D., Hess, K.U., Dingwell, D.B., 2018. Shear rate-dependent disequilibrium rheology and dynamics of basalt solidification. Geophys. Res. Lett. 45, 6466–6475.
Kolzenburg, S., Giordano, D., Di Muro, A., Dingwell, D.B., 2019. Equilibrium viscosity and disequilibrium rheology of high magnesium basalt from Piton de la Fournaise volcano, La Reunion, Indian Ocean, France. Annals of Geophysics 62 (2), VO218. https://doi.org/10.4401/ag-7839, 2019.
Kolzenburg, S., Hess, K.U., Berlo, K., Dingwell, D.B., 2020. Disequilibrium rheology and crystallization kinetics of basalts and implications for the phlegrean volcanic district front. Earth Sci 8, 187. https://doi.org/10.3389/feart.2020.00187.
Kouchi, A., Tsuchiyama, A., Sunagawa, I., 1986. Effect of strirring on crystallization kinetics of basalt: texture and elements patitioning. Contribut. Mineral. Petrol. 93, 429–438.
Li, X., Zhang, C., Behrens, H., Holtz, F., 2020. Calculating biotite formula from electron microprobe analysis data using a machine learning method based on principal components regression. Lithos 356–357, 105371 (2020).
Marsh, B.D., 1988a. Crystal capture, sorting, and retention in convecting magma. Geol. Soc. Am. Bull. 100, 1720–1737.
Marsh, B.D., 1988b. Crystal size distribution (CSD) in rocks and the kinetics and dynamics of crystallization I. Theory. Contrib. Mineral. Petrol. 99, 277–291.
Mezner, T.G., 2014. The Rheology Handbook—For Users of rota- tional and Oscillatory Rheometers, 4th edn. Vincentz Network, Hanover.
Mills, R.D., Glazner, A.F., 2013. Experimental study on the effects of temperature cycling on coarsening of plagioclase and olivine in an alkali basalt. Contrib Miner Petrol 166, 97–111.
Mollo, S., Blundy, J., Scarlato, P., De Cristofaro, S.P., Tecchiato, V., Di Stefano, F., Vetere, F., Holtz, F., Bachmann, O., 2018. An integrated P-T-H2O-lattice strain model to quantify the role of clinopyroxene fractionation on REE+Y/HFSE patterns of mafic alkaline magmas: application to eruptions at Mt. Etna. Earth Sci. Rev. 185, 32–56.
Mollo, S., Hammer, J.E., 2017. Dynamic crystallization in magmas. In: Heinrich, W., Abart, R. (Eds.), Mineral Reaction Kinetics: Microstructures, Textures, Chemical and Isotopic Signatures. EMU Notes in Mineralogy, pp. 1–46, 16Published by the European Mineralogical Union and the Mineralogical Society of Great Britain & Ireland.
Mollo, S., Pontesilli, A., Moschini, P., Palummo, F., Taddeucci, J., Andronico, D., Del Bello, E., Scarlato, P., 2022. Modeling the crystallization conditions of clinopyroxene crystals erupted during February–April 2021 lava fountains at Mt. Etna: Implications for the dynamic transfer of magmas. Lithos 420–421, 106710. https://doi.org/10.1016/j.lithos.2022.106710.
Mollo, S., Moschini, P., Ubide, T., MacDonald, A., Vetere, F., Nazzari, M., Misiti, V., Miyajimae, N., Melai, C., Di Genova, D., Vona, A., Di Fiore, F., Romano, C., 2023. Kinetic partitioning of trace cations between zoned clinopyroxene and a variably cooled-decompressed alkali basalt: thermodynamic considerations on lattice strain and electrostatic energies of substitution. Geochim. Cosmochim. Acta 361, 40–66 (2023).
Morgavi, D., Petrelli, M., Vetere, F., González-García, D., Perugini, D., 2015. High-temperature apparatus for chaotic mixing of natural silicate melts. Rev. Scintific Instrum. 86, 105108.
Mueller, S., Llewellin, E.W., Mader, H.M., 2010. The rheology of suspensions of solid particles. Proceedings of the Royal Society A: Math., Phys. Eng. Sci. 466, 1201–1228. https://doi.org/10.1098/rspa.2009.0445.
Musu, A., Corsaro, R.A., Higgins, O., Jorgenson, C., Petrelli, M., Caricchi, L., 2023. The magmatic evolution of South-East Crater (Mt. Etna) during the February–April 2021 sequence of lava fountains from a mineral chemistry perspective. Bull. Volcanol. 85, 33. Springer.
Nicolas, A., Ildefonse, B., 1996. Flow mechanism and viscosity in basaltic magma chambers. Geophys. Res. Lett. 23 (16), 2013–2016. https://doi.org/10.1029/96GL02073.
Papale, P., 1999. Strain-induced magma fragmentation in explosive eruptions. Nature 397 (6718), 425–428. https://doi.org/10.1038/17109.
Petrelli, M., El Omari, K., Le Guer, Y., Perugini, D., 2016. Effects of chaotic advection on the timescales of cooling and crystallization of magma bodies at mid crustal levels. Geochem. Geophys. Geosyst. 17 (Issue 2), 425–441.
Piombo, A., Dragoni, M., 2009. Evaluation of flow rate for a one-dimensional lava flow with power-law rheology. Geophys. Res. Lett. 36, L22306. https://doi.org/10.1029/2009GL041024.
Pistone, M., Cordonnier, B., Ulmer, P., Caricchi, L., 2016. Rheological flow laws for multiphase magmas: an empirical approach. J. Volcanol. Geotherm. Res.
Polacci, M., Arzilli, F., La Spina, G., Le Gall, N., Cai, B., Hartley, M.E., Di Genova, D., Vo, N.T., Nonni, S., Atwood, R.C., Llewellin, E.W., 2018. Crystallisation in basaltic magmas revealed via in situ 4D synchrotron X-ray microtomography. Sci. Rep. 8, 1–13.
Pupier, E., Duchene, S., Toplis, M., 2008. Experimental quantification of plagioclase crystal size distribution during cooling of a basaltic liquid. Contrib. Mineral. Petrol. 155, 555–570. https://doi.org/10.1007/s00410-007-0258-9.
Putirka, K.D., 2017. Down the crater: where magmas are stored and why they erupt. Elements 13, 11–16. https://doi.org/10.2113/gselements.13.1.11.
Richet, P., Lejeune, A.M., Holtz, F., Roux, J., 1996. Water and the viscosity of andesite melts. Chem. Geol. 128 (1–4), 185–197.
Rusiecka, M.K., Bilodeau, M., Baker, D.R., 2020. Quantification of nucleation delay in magmatic systems: experimental and theoretical approach. Contrib. Mineral. Petrol. 175 (5), 47.
Shea, T., Hammer, J.E., 2013. Kinetics of cooling- and decompression-induced crystallization in hydrous mafic-intermediate magmas. J. Vocanol. Geotherm. Res. 260, 127–145. https://doi.org/10.1016/j.jvolgeores.2013.04.018.
Spina, L., Cimarelli, C., Scheu, B., Di Genova, D., Dingwell, D.B., 2016a. On the slow decompressive response of volatile- and crystal-bearing magmas: an analogue experimental investigation. Earth Planet. Sci. Lett. 433, 44–53.
Spina, L., Scheu, B., Cimarelli, C., Arciniega-Ceballos, A., Dingwell, D.B., 2016b. Time scales of foam stability in shal- low conduits: insights from analogue experiments. Geochem. Geophys. Geosyst. 17 (10), 4179–4194.
Tripoli, B., Manga, M., Mayeux, J., Barnard, H., 2019. The effects of deformation on the early crystallization kinetics of Basaltic Magmas. Front. Earth Sci. 7, 250. https://doi.org/10.3389/feart.2019.00250.
Vetere F. and Holtz F. (2020) Rheological behaviour of partly crystallized silicate melts under variable shear rate. Chapter in Dynamic Magma Evolution, Geophysical Monograph Series – WILEY, edited by Vetere F.
Vetere, F., Iezzi, G., Behrens, H., Holtz, F., Ventura, G., Misiti, V., Cavallo, A., Mollo, S., Dietrich, M., 2015. Glass forming ability and crystallization behaviour of sub-alkaline silicate melts. Earth Science Review 150, 25–44. https://doi.org/10.1016/j.earscirev.2015.07.001.
Vetere, F., Iezzi, G., Perugini, D., Holtz, F., 2022. Rheological changes in melt and magma induced by deformation and cooling events. CR-Geosciences 354, 1–22. https://doi.org/10.5802/crgeos.125.
Vetere, F., Murri, M., Alvaro, M., Domeneghetti, M.C., Rossi, S., Pisello, A., Holtz, F., Perugini, D., 2019. Viscosity of pyroxenite melt and its evolution during cooling: an experimental approach. JGR-Planets 124. https://doi.org/10.1029/2018JE005851.
Vetere, F., Petrelli, M., Perugini, D., Haselbach, S., Morgavi, D., Pisello, A., Iezzi, G., Holtz, F., 2021. Rheological evolution of eruptible Basaltic-Andesite Magmas under dynamic conditions: the importance of plagioclase growth rates. J. Volcanol. Geotherm. Res. 420, 107411.
Vetere, F., Rossi, S., Namur, O., Perugini, D., Morgavi, D., Misiti, V., Mancinelli, P., Petrelli, M., Pauselli, C., 2017. Experimental constraints on the rheology, eruption and the rheology, eruption and emplacement dynamics of lavas from Mercury Northern Volcanic Plains. J. Geophys. Res. – Planets 122, 1–17. https://doi.org/10.1002/2016JE005181.
Vetere, F., Sato, H., Ishibashi, H., De Rosa, R., Donato, P., 2013. Viscosity changes during crystallization in shoshonitic magma: new insight on the lava flow emplacement. J. Mineral. Petrol. Sci. 108 (3), 144–160.
Vona, A., Romano, C., 2013. The effects of undercooling and deformation rates on the crystallization kinetics of Stromboli and Etna basalts. Contrib. Mineral. Petrol. 166, 491–509. https://doi.org/10.1007/s00410-013-0887-0.
Vona, A., Romano, C., Dingwell, D.B., Giordano, D., 2011. The rheology of crystal-bearing basaltic magmas from Stromboli and Etna. Geochim. Cosmochim. Acta 75 (11), 3214–3236. https://doi.org/10.1016/j.gca.2011.03.031.
Whittington, A., Richet, P., Holtz, F., 2000. Water and the viscosity of depolymerized aluminosilicate melts. Geochimica et Cosmochi- mica Acta 64 (21), 3725–3736.
Whittington, A., Richet, P., Linard, Y., Holtz, F., 2001. The viscosity of hydrous phonolites and trachytes. Chem. Geol. 174 (1–3), 209–223.